Review of Scientific Instruments

Time-resolved thermally induced aberrations in a flash-lamp pumped Nd:Glass disk amplifier using a 2 × 2 position sensitive detector array

Cite as: Rev. Sci. Instrum. **90**, 123106 (2019); https://doi.org/10.1063/1.5120388
Submitted: 30 July 2019 • Accepted: 10 November 2019 • Published Online: 06 December 2019

M. Ahmad, M. Galletti, P. Oliveira, et al.

AIP Publishing

Review of Scientific Instruments ARTICLE scitation.org/journal/rsi

Time-resolved thermally induced aberrations in a flash-lamp pumped Nd:Glass disk amplifier using a 2 × 2 position sensitive detector array

Cite as: Rev. Sci. Instrum. 90, 123106 (2019); doi: 10.1063/1.5120388
Submitted: 30 July 2019 • Accepted: 10 November 2019 •
Published Online: 6 December 2019

M. Ahmad,[1,2,a)] M. Galletti,[2,3] P. Oliveira,[2] E. Dilworth,[2,4] D. J. Robinson,[2] M. Galimberti,[2] A. J. Crawford,[5] I. Musgrave,[2] and M. J. D. Esser[1]

AFFILIATIONS

[1]School of Engineering and Physical Sciences, Heriot-Watt University, Edinburgh EH14 4AS, United Kingdom
[2]Central Laser Facility, Science and Technology Facilities Council, Rutherford Appleton Laboratory, Harwell Science and Innovation Campus, Didcot OX11 0QX, United Kingdom
[3]GoLP Instituto de Plasmas e Fusão Nuclear, Instituto Superior Tecnico, Universidade de Lisboa, Av. Rovisco Pais, 1049-001 Lisbon, Portugal
[4]Department of Mathematical Sciences, University of Bath, Bath BA2 7AY, United Kingdom
[5]Université Bordeaux 1, Département de Physique, 351 Cours de la Libération, 33400 Talence, France

[a)]**Electronic mail:** munadi.ahmad@stfc.ac.uk

ABSTRACT

A novel technique of measuring the prompt, thermally induced wave-front aberrations in a large aperture flash-lamp pumped Nd^{3+} glass disk amplifier is presented. Implementing a 2 × 2 lens array and a 2 × 2 position sensitive detector array as a diagnostic system, the wave-front profile was successfully reconstructed for the first five Zernike terms for a temporal window of 8.5 ms.

I. INTRODUCTION

Petawatt class Nd:glass laser facilities, such as the Vulcan laser system at the Central Laser Facility (CLF, RAL), often rely on large aperture flash-lamp pumped disk amplifiers to generate high energy laser pulses. Flash-lamps, as pumping sources, offer many advantages; their broad spectrum is suitable when pumping large Nd:glass disks with five separate pump bands and they are an inexpensive method of providing high pump energy.[1] Because of these properties, they are widely implemented in various high power laser systems, despite their inefficiency in converting input energy to useful extracted energy required for pumping. Flash-lamps induce a considerable amount of thermal loading in Nd:glass amplifiers. Many factors contribute to the thermal loading of the disk amplifiers; perhaps the largest contribution is due to the quantum defect. The quantum defect is the difference in energy between the pumping photons and the amplified laser photons. Other contributions include the quantum efficiency term which determines the efficiency of pump photons that contribute to the population inversion[2,3] in the amplifier and absorption due to impurities present in the disk amplifier. A detailed study on the heating contributions in Nd:glass is presented in the work of Koechner.[4] The thermal loading in the disks lead to thermally aberrated laser beams reducing the focal spot intensity needed for high intensity experiments. The time needed to recover the focal spot intensity severely limits the systems repetition rate (e.g., 1PW Vulcan laser system with a recovery time of ~30 min[5]). Due to the geometry of the disk amplifier used, flash-lamps provide a nonuniform intensity distribution on the disk amplifiers, which leads to a temperature gradient being formed along the disk amplifiers. An increase in temperature causes the disks to expand due to the thermal expansion coefficient α_T and causes a change in the refractive index $\boldsymbol{n}$ due to the thermo-optic coefficient $d\boldsymbol{n}/dT$. The relationship between the change in optical path length ΔOPL and temperature ΔT is as follows[6] (neglecting

effects from stress induced components):

$$\Delta OPL(x,y,z) = \left(\frac{d\mathbf{n}}{dT} + \alpha_T(n-1)\right)\int_0^L \Delta T(x,y,z)\quad dz.$$

A laser beam propagating through a medium with a temperature gradient will experience a nonuniform change in the optical path length, which results in an aberrated beam. Thermally induced wave-front aberrations are categorized into two broad categories: the prompt aberrations, which are usually within the microsecond to millisecond and the temporal regime, and the long lasting thermal aberrations, which can last for several minutes to hours. The long lasting thermal aberrations ultimately limits the repetition rate of the laser system and are dependent on the heat transfer mechanisms occurring within the whole disk amplifier system. Convective heating from the heated flashlamps to the disk amplifier cavity and the conductive heating from the disk cladding to the glass disks both contribute toward the long lasting thermal aberrations.[7,8] The prompt aberrations, which are the subject of the paper, can be a real concern due to their fast build-up time, which means they cannot be actively corrected for using traditional adaptive optics techniques. They are usually precompensated for; therefore, accurately determining the nature of these aberrations becomes essential.

The results presented in this paper are based on a large aperture disk amplifier, which consists of six Nd:glass disks pumped by two sets of four flash-lamps. The six 230 × 115 mm^2 elliptical disks are mounted at Brewster's angle. A Nd doped phosphate glass with a 323 μs radiative lifetime (Schott US-LG-760) is used in the disk amplifier. The disks become thermally loaded as soon as the flashlamp pulse starts and peaks at approximately 374 μs, and the energy stored for laser amplification peaks at approximately ~600 μs for the disk amplifier used in this study. This study will define an efficiency factor χ_a, which takes into account the focal beam quality due to the thermal loading (Strehl ratio) and the small signal gain in the amplifier. The efficiency factor is defined as

$$\chi_a = GS, \tag{1}$$

where G is the small signal gain and S is the Strehl ratio. The Strehl ratio is defined as the ratio of the on-axis intensity of a focused beam and the theoretical intensity of an unaberrated focused beam.[9] We adopt Mahajan's definition of the Strehl ratio, which varies exponentially with the rms wave-front error squared,[10]

$$S = e^{-4\pi^2\sigma^2}.$$

Attempts have been made to understand a similar parameter of the Strehl efficiency factor, called the heating parameter, which is defined as the ratio of energy stored for amplification to the heat energy in the amplifier.[2,11] An increase in temperature does not necessarily mean that the beam propagating through the medium becomes aberrated. The temperature gradient results in the optical path length of the beam changing nonuniformly, which is why an efficiency factor taking into account the rms wave-front error is more meaningful.

II. WAVE-FRONT SENSING TECHNIQUES

A variety of instruments can be used to detect wave-front aberrations; common techniques include a Shack-Hartmann Wave-front Sensor (SH-WFS) and interferometric techniques. A SH-WFS usually consists of a microlens array, which produces an array of far field spots on a camera. An aberrated beam causes the position of the far field spots produced by the microlens array to deviate from the reference position. Measuring the change in the position of the far field spots produced by the microlens array enables the wave-front to be reconstructed. A major advantage of using such a technique is the design's compactness and its ability to solve for higher order Zernike terms.[12] Interferometry is another common approach to measure the wave-front aberrations; the interference pattern produced by a reference beam interfering with an aberrated beam is used to detect the change in the optical path length between the two beams.[13] The interference pattern is projected onto a camera, which relies on image analysis tools to derive the wave-front aberrations.

Both SH-WFS and interferometric techniques have limited temporal resolution due to the frame rate that can be reasonably achieved from imaging cameras.

To overcome this problem, previous researchers have captured large temporal windows in small time intervals by triggering a SH-WFS at different time intervals after the pump pulse. This technique has been demonstrated for a 1 ms diode pumped Yb:YAG slab. A pulsed fiber-coupled probe at 936.6 nm was used to probe a Yb:YAG slab, and a SH-WFS was used to gather data at a series of points along the temporal window.[14] However, this method would be difficult to implement in a flash-lamp pumped Nd:glass system due to the variations in parameters from shot to shot and the low repetition rate.[5]

An alternative method of wave-front sensing used in astronomy is the pyramid wave-front sensor, which was first proposed by Ragazzoni.[15] A pyramid wave-front sensor consists of a transparent pyramid, which divides the laser beam into four segments. To increase the number of data points, the laser beam is modulated by circling the tip of the transparent pyramid. The four fields created by the pyramid are projected on either a CMOS/CCD camera or a photodiode array. The displacement of the four spot fields is used to reconstruct the wave-front.[16]

In this paper, we present an alternative technique implementing four lenses and four PSDs (Position Sensitive Detectors) in 2 × 2 arrays. The main advantage of using PSDs instead of an imaging camera is the increase in temporal resolution. With just four lenses and four PSDs, only eight data points can be evaluated per temporal frame (four in the x-axis and four in the y-axis). In the context of flash-lamp pumped large aperture Nd:glass amplifiers, the evaluation of the first five Zernike terms is sufficient as the contribution from the higher order terms is much smaller in comparison.[5]

III. POSITION SENSITIVE DETECTORS (PSDs)

A lateral effect PSD was used in this study due to its insensitivity to noncircular beam shapes and its ability to detect small diameter beams in comparison with the quad-cell PSD. However, a quad cell PSD can provide a temporal resolution of up to 150 kHz as opposed to the lateral effect PSD, which is limited to 15 kHz.

A lateral effect PSD detector consists of a photo resistive layer with four points in the corners, A, B, C, and D, as shown in Fig. 1. The photocurrents measured at the four points are used to

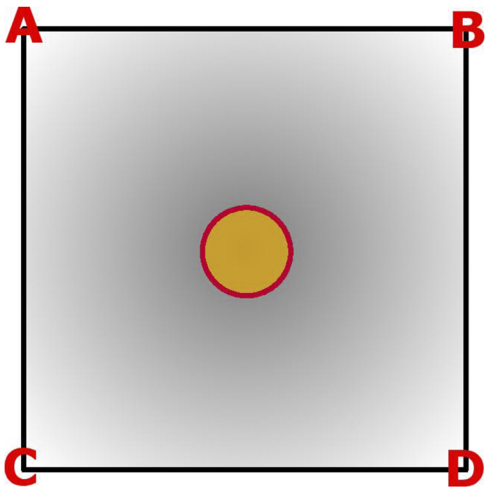

FIG. 1. Lateral effect PSD detector.

determine the position of the beam. The position of the beam in the y-axis is determined by the magnitude of the current detected in the points A and B with respect to C and D. The position in the x-axis is determined by the magnitude of the current detected in the points A and C with respect to B and D. A normalization factor *SUM* is used to account for the total intensity per measurement,

$$\begin{aligned} \Delta x &= (A + C) - (B + D), \\ \Delta y &= (A + B) - (C + D), \\ SUM &= (A + B) + (C + D). \end{aligned} \tag{2}$$

In order to calculate the change in position of the beam in units of distance, x_D and y_D, the size of the detector L_x and L_y must be taken into account (PSD Thorlabs-PDP90A $L_x = L_y = 10$ mm),

$$x_D = \frac{L_x \Delta x}{2SUM}, \quad y_D = \frac{L_y \Delta y}{2SUM}. \tag{3}$$

The thermally induced aberrations can be measured using the amplified laser beam or a probe beam with a wavelength outside the gain bandwidth of the amplifier. The SUM output term should be measured simultaneously as it increases by up to a factor of 9 (in our case, the small signal gain is ~9) during amplification if the amplified laser beam is used.

IV. EXPERIMENTAL SETUP

A schematic of the optical layout is shown in Fig. 2, illustrating the experimental setup of the Vulcan beam line which was used

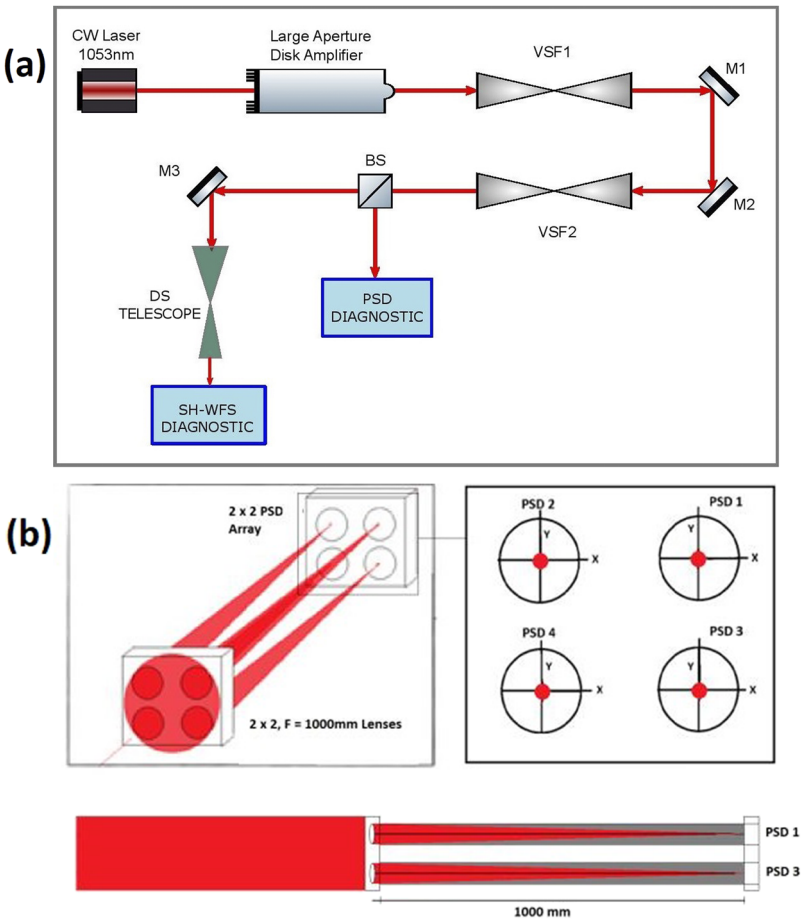

FIG. 2. (a) Optical layout of measuring the prompt, thermally induced aberrations in a large aperture disk amplifier using a PSD wave-front sensor where BS is a beam splitter. (b) Optical layout of the PSD diagnostics as shown in (a).

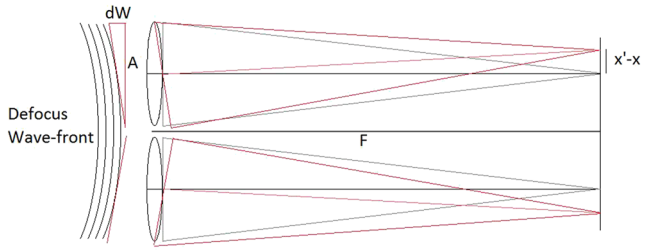

FIG. 3. A defocused wave-front compared with a planar wave-front incident on the PSD array through a lens array placed at a distance F, which is the focal length of the lens array.

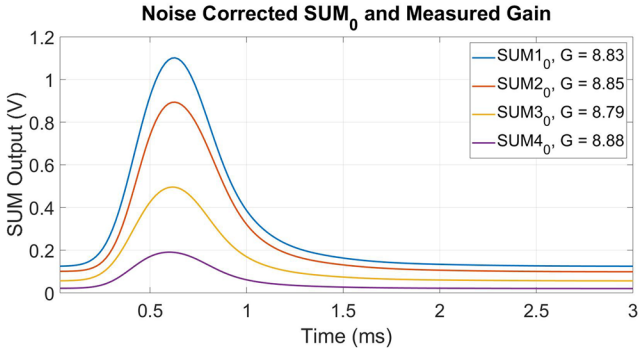

FIG. 4. Noise corrected SUM outputs in volts for PSD 1, PSD 2, PSD 3, and PSD 4 and the calculated gain for the four SUM outputs. Different neutral density filters were used for each PSD detector to control the maximum intensity incident upon the PSD detectors.

to investigate the temporal change in thermal aberrations of the large aperture disk amplifier. A 1053 nm continuous wavelength (CW) beam was used for the measurements. A 96 mm diameter beam is amplified by the large aperture disk amplifier, before traveling through a Vacuum Spatial Filter (VSF1), which is designed to increase the diameter of the beam from 96 mm to 108 mm. Beyond VSF1, the beam is reflected off two HR mirrors at 45°, before it propagates through the second VSF (VSF2). The pinhole size in the VSFs are orders of magnitude larger than the diffraction limited spot of the CW. Beyond VSF2, the beam enters a beam splitter (BS). The reflected beam enters the PSD diagnostics, while the transmitted is further reflected off another 45° HR mirror and downsized before going into the SH-WFS diagnostics. In the PSD diagnostics, the CW beam enters the 2 × 2 lens array of 1 in., f = 1000 mm, lenses. The four 1 in. segments of the beam are focused on to four separate PSDs, as shown in the bottom of Fig. 2. The initial positions of the focal spots on the PSD array prior to the firing of the flash-lamps were used as the reference position. After the flash-lamps have fired, the thermally aberrated beam causes the focal spot positions on the PSDs to deviate from the reference position. The change in the position of the focal spots with respect to the reference position is directly proportional to the first derivative of the wave-front. A 2D representation of a defocused beam entering the PSD diagnostics is shown in Fig. 3. The change in the focal spot position is measured simultaneously with the gain. The temporal profile of the gain was measured using just the SUM output of the four PSDs.

V. SOURCES OF NOISE

Amplified Spontaneous Emission (ASE) propagating in the same direction as the amplified laser beam can introduce noise in the measurements. Filtering out the spontaneous emission proved to be a difficult task as it temporally and spectrally overlaps with the laser beam. If the gain of the disk amplifiers is known, then ASE contributions can simply be subtracted from the original data. The movement detected by the PSDs in the x and y directions due to noise was measured by firing the flash-lamps while blocking the CW from entering the disk amplifier. Once the noise was removed from the measurements, the ratio of the peak of the SUM output and the SUM output of the unamplified CW beam was in good agreement with the overall gain of the amplifier (~9). This treatment is only possible if there is a linear relationship between the PSDs SUM, X, and Y outputs. According to Eq. (2), we can write A, B, C, and D as data points without noise, and ϵ_A, ϵ_B, ϵ_C, and ϵ_D as the noise contribution to the measurements A_m, B_m, C_m, and D_m,

$$\begin{aligned} A_m &= A + \epsilon_A, \\ B_m &= B + \epsilon_B, \\ C_m &= C + \epsilon_C, \\ D_m &= D + \epsilon_D. \end{aligned} \tag{4}$$

The total sum of the noise contributions ϵ_A, ϵ_B, ϵ_C, and ϵ_D is ϵ_{SUM}. The measured SUM output, SUM_m, therefore consists of the data SUM and the SUM contribution from the noise ϵ_{SUM}; $SUM_m = SUM + \epsilon_{SUM}$. Due to the linear relationship between the three outputs of the PSDs, a similar treatment can be used for the X and Y movements, where the movement in the X and Y directions due to the noise is ϵ_x and ϵ_y,

$$\begin{aligned} \epsilon_x &= (\epsilon_A + \epsilon_C) - (\epsilon_B + \epsilon_D), \\ \epsilon_y &= (\epsilon_A + \epsilon_B) - (\epsilon_C + \epsilon_D), \\ \Delta x_m &= \Delta x + \epsilon_x, \\ \Delta y_m &= \Delta y + \epsilon_y. \end{aligned} \tag{5}$$

The noise corrected SUM outputs for all four PSDs are shown in Fig. 4. In order to verify the analysis, the maximum gain was measured for the SUM outputs by taking the ratio of the measured voltage for the unamplified beam and the registered peak voltage. All SUM outputs for the four PSDs had a measured gain of approximately 9, which is in good agreement with the total gain of the disk amplifier being used (Fig. 5).

VI. ANALYSIS

At ~615 μs, the energy stored in the upper laser is maximized for the disk amplifier used in our study. Due to the heating processes discussed in the Introduction, the Nd:glass material is thermally loaded, which causes the amplified beam passing through the medium to become aberrated. Using the small angle approximation, the gradient of the wave-front profile is proportional to the change

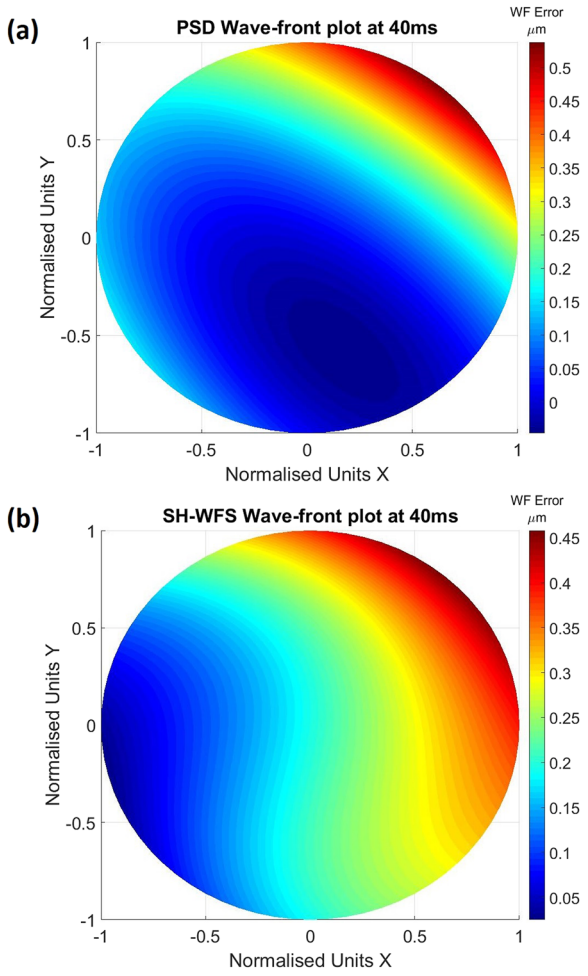

FIG. 5. (a) Wave-front reconstruction from the experimental setup of four PSDs at 40 ms after the beginning of the flash-lamp pulse. (b) SH-WFS wave-front plot from 15 Zernike coefficients at 40 ms after the beginning of the flash-lamp pulse.

in the focal spot position measured with the PSDs,[17]

$$\frac{dW(x,y)}{dx}\Big|_{x=x_0} = \frac{x' - x_R(x_0)}{2f},$$
$$\frac{dW(x,y)}{dy}\Big|_{y=y_0} = \frac{y' - y_R(y_0)}{2f}, \tag{6}$$

where the wave-front of the aberrated beam is W(x, y), the focal length of the 2 × 2 lens array is f, the central position of a lens in the lens array is (x_0, y_0), the reference position measured using the reference beam is denoted as $x_R(x_0)$ and $y_R(y_0)$, and the position measured with the aberrated beam is x' and y'.

For each of the four PSDs in the array, two differential equations are generated. In total, eight equations can be used to reconstruct the wave-front profile (see the Appendix).

Earlier research in characterizing the wave-front profile performed in Vulcan[5] shows that during the recovery period after a shot (time needed for the wave-front to fully recover), astigmatism and defocus were the dominant aberrations. Therefore, the only Zernike terms considered in the reconstruction of the wave-front are shown in Table I. Using the Zernike polynomials in their Cartesian form, the wave-front can be reconstructed, adopting the 5 Zernike terms shown in Table I, as follows:[18]

TABLE I. Zernike terms (piston excluded) included in the reconstruction of the wave-front.[18]

n	m	Cartesian form	Zernike term
1	−1	x	Tip
1	1	y	Tilt
2	2	2xy	Astigmatism 45°
2	0	$-1 + 2x^2 + 2y^2$	Defocus
2	−2	$-x^2 + y^2$	Astigmatism 0°

$$W(x,y) = 2Z_a x + 2Z_b y + 2\sqrt{6}Z_c xy + \sqrt{3}Z_d(-1 + 2x^2 + 2y^2) + \sqrt{6}Z_e(x^2 - y^2). \tag{7}$$

The Z_a, Z_b, Z_c, Z_d, and Z_e fitting constants can be evaluated using the differential equations in Eq. (6). The least squares fit method was used to retrieve the fitting constants (see the Appendix). In order to normalize the Zernike coefficients, the coordinate system was changed from Cartesian to polar co-ordinates, where ρ_0 is the radius of the beam,

$$Z_{a,n} = \frac{Z_a}{\rho_0}, \quad Z_{b,n} = \frac{Z_b}{\rho_0},$$
$$Z_{c,n} = \frac{Z_c}{\rho_0^2}, \quad Z_{d,n} = \frac{Z_d}{\rho_0^2}, \quad Z_{e,n} = \frac{Z_e}{\rho_0^2}. \tag{8}$$

The piston is a constant value that offsets the wave-front profile by a constant value and is determined by the central position of the wave-front profile.

VII. COMPARISON WITH SH-WFS

The validity of the experimental data and the mathematical analysis was confirmed by a wave-front profile derived from the Thorlabs (WFS30-5C) SH-WFS sensor. The PSD diagnostics and the SH-WFS were used for a single data point. An 80 ms scan of the focal spot movement was carried out to find a region of stability, where the focal spot movements are relatively constant over a 10 ms time period. A 10 ms time period was used to match the exposure time set on the SH-WFS. At 40 ms, the PSD diagnostics and the SH-WFS were triggered. The change in the focal spot positions measured with the PSDs was used to reconstruct the wave-front profile. The wave-front profile derived from the SH-WFS was used to compare the wave-front profile derived from the PSD diagnostics. The wave-front reconstruction using the data from the PSDs was fitted to the first 5 Zernike terms, and the data from the SH-WFS were also fitted to the first 5 Zernike terms. The focal spot movements detected for the four PSDs show a Peak-Valley (PV) wave-front error of approximately 0.5 μm. The peak to valley measured for SH-WFS is in the order of 0.45 μm.

Both plots show a larger optical path length with respect to the reference beam on the top right hand corner of the profile. The slight

discrepancy between the shapes of the profile is due to the pupil positioning for the PSDs.

VIII. RESULTS AND DISCUSSION

An 8.5 ms temporal window was selected for the measurements with a temporal resolution of 17 μs. The reference positions on the PSDs were acquired by measuring the SUM, X, and Y output for all four PSDs prior to the triggering of the flash-lamps. The X and Y positions of the beam were measured after the flash-lamp trigger and compared to the reference positions. The X and Y positions of the focal spot measured for the PSDs are shown in Fig. 6. The peak movement detected in Fig. 6 is around the 250 μs–1 ms region, which coincides with the peak current of the flash-lamp pulse at 273 μs

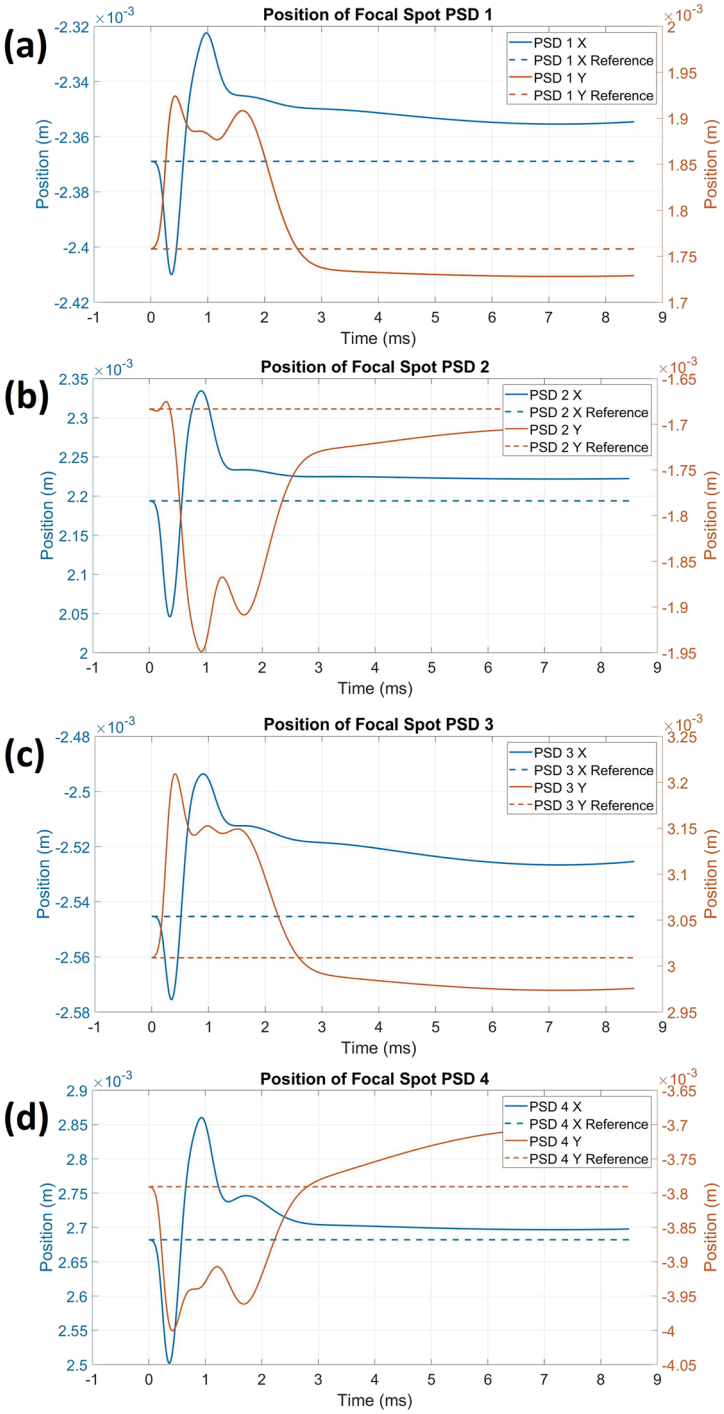

FIG. 6. (a) PSD1, (b) PSD2, (c) PSD3, and (d) PSD4. The position of the X and Y movements measured for all PSDs. The X and Y reference positions were measured prior to the flash-lamp trigger.

and the length of the flash-lamp pulse which is approximately 1 ms long.

At approximately 3 ms, the gradient of the focal spot positions gradually become smaller and it approaches a relatively stable position. To further analyze the behavior of the thermal aberrations in the disk amplifier, the least squares fit method was used to derive the Zernike coefficients and the rms wave-front error, both as functions of time. The dominant aberration measured is astigmatism at 0°, which peaks at 373 μs. Defocus and astigmatism at 45° also peak at 373 μs but are less prominent than the astigmatism term at 0°. The rms wave-front error was calculated using the reconstructed wave-front profile,

$$\sigma(t)^2 = \frac{1}{A}\int\left[W(x,y,t)^2 - \overline{W(x,y,t)}^2\right]dxdy, \qquad RMS = \sigma. \tag{9}$$

The rms is a good indication of the relative "flatness" of the wave-front profile. It is an indication of how the values specified at each point in the wave-profile $W(x, y, t)$ deviate from the calculated mean value of the profile $\overline{W(x,y,t)}$ in the x and y direction for each point in time.

This represents the overall quantitative description of how thermal aberrations change over time. Using the least squares fit method, the Zernike coefficients were derived from the PSDs. The Zernike coefficients were used to plot the wave-front profile at each time step, and the rms wave-front error and the Strehl ratio were calculated from the Zernike coefficients.

Three distinct peaks can be observed from the rms wave-front error plot in Fig. 7.

The heights of the three peaks are approximately 0.06 μm, and the difference in the peak to trough value for the three peaks is approximately 0.01 μm, therefore considered to be insignificant for any physical analysis. However, a sharp decrease in the rms error is observed between 1.7 ms and 2.7 ms. This would suggest that the temperature gradient along the disk amplifier decreases considerably, improving the overall rms error. From Fig. 7, astigmatism at 0° also decreases during 1.7 ms–2.7 ms which suggests that the sudden improvement in the rms error is due to the recovery of the astigmatism term.

As shown in Fig. 4, at 615 μs, the energy stored for laser amplification is maximized and the corresponding rms wave-front error is measured to be 0.05 μm. The wave-front profile at 374 μs, 615 μs, 918 μs, 2.65 ms, and 8.5 ms is plotted in Figs. 8 and 9, for comparison with the rms wave-front error in Fig. 7. At 374 μs until 2.65 ms after the trigger of the flash-lamps, the wave-front profile suffers from astigmatism mostly which can also be observed in Fig. 10.

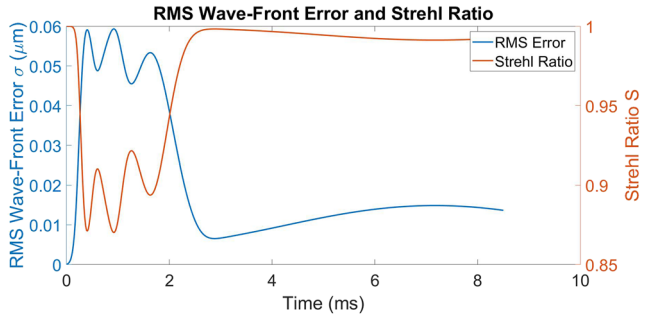

FIG. 7. RMS wave-front error and the Strehl ratio plotted as a function of time.

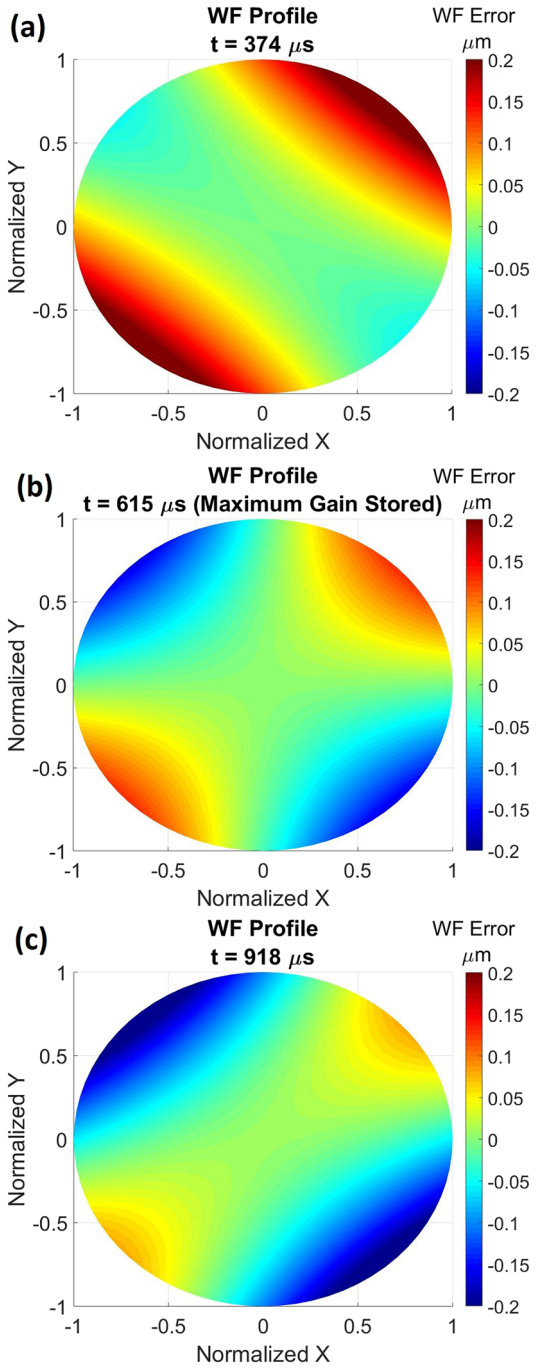

FIG. 8. Wave-front profile measured at (a) 374 μs, (b) 615 μs, and (c) 918 μs. The wave-front error measured in μm is the same for all plots in order to show the evolution of the wave-front profile from 374 μs onward.

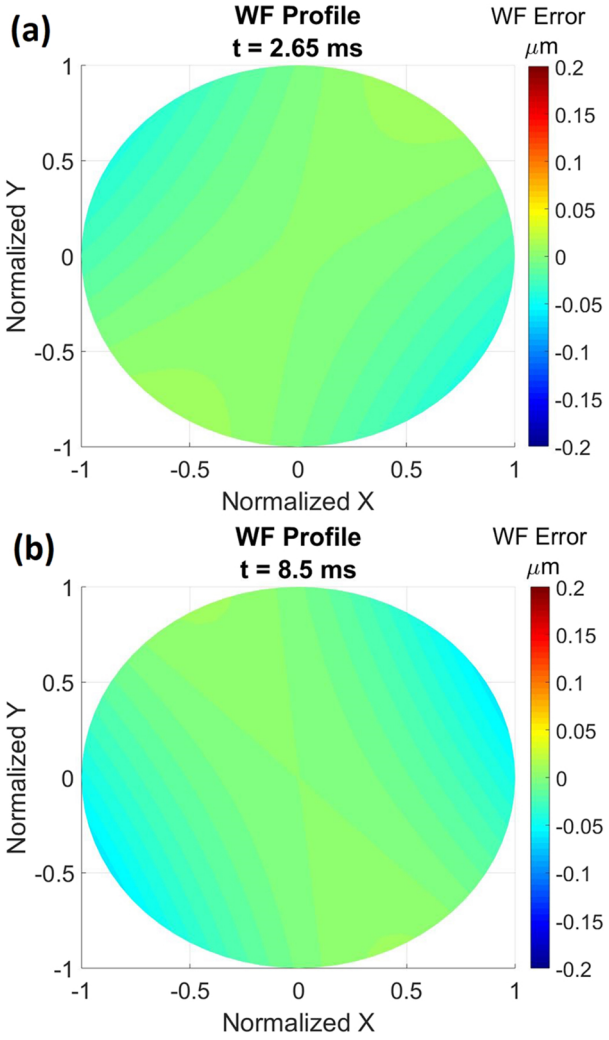

FIG. 9. Wave-front profile measured at (a) 2.65 ms and (b) 8.5 ms. The wave-front error measured in μm is the same for all plots in order to show the evolution of the wave-front profile from 2.65 ms onward.

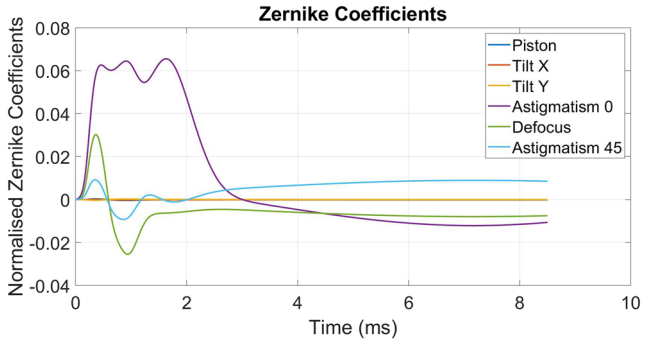

FIG. 10. Zernike coefficients derived using the least squares fit method. Change in piston, tilt X, tilt Y, astigmatism (0° and 45°), and defocus as a function of time.

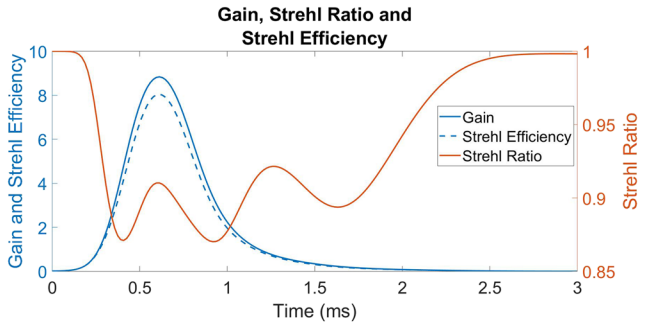

FIG. 11. The efficiency factor is shown as a blue dashed line, the Strehl ratio is shown as a red solid line, and the small signal gain is shown as a blue solid line. The maximum Strehl efficiency that can be achieved is 7.9 for a small signal gain of 8.82.

The peak-valley at 374 μs is approximately 0.25 μm, which decreases to 0.2 μm at 918 μs. At 2.65 ms, an appreciable decrease in astigmatism and the rms wave-front error is seen in Figs. 10 and 7; the wave-front profile at 2.65 ms shows a peak-valley wave-front error of just 0.05 μm. At approximately 3 ms, the dominant astigmatism term becomes negative, hence rotating the astigmatism axis as shown for 8.5 ms in Fig. 9. Whether the wave-front error is stable beyond 8.5 ms is not yet known; however, from previous studies, we know that the thermal aberrations continue to be present for ~30 min.[5] According to Fig. 11, the most efficient time to extract the stored energy for laser amplification is at 615 μs, which corresponds to the temporal peak of the gain.

The efficiency increases with the gain profile until 374 μs, which is when the rms wave-front error is at its maximum. Beyond 374 μs, the efficiency curve drops below the small signal gain.

When extracting lower energies, it is more efficient to extract before the peak of the gain as opposed to after. This can be seen by observing the difference between the small signal gain curve and the efficiency curve—the gap between the two curves is larger after the peak of the gain curve as opposed to before the peak of the gain curve. The Strehl ratio efficiency for this particular disk amplifier geometry is 7.9.

IX. CONCLUSION

A novel technique to measure the prompt, thermally induced wave-front aberrations with a high temporal resolution is demonstrated for a large aperture, flash-lamp pumped Nd:glass amplifier. The system consists of a 2 × 2 lens array focusing four portions of the beam into a 2 × 2 PSD array. The change in the centroid position of the aberrated beam with respect to the reference beam was measured using the PSDs. A least squares fit method was implemented to fit the Zernike coefficients to measured PSD data, the rms wave-front error was calculated for each time step, and the wave-front efficiency factor was derived and analyzed. Using an efficiency factor as in Eq. (1), it is a meaningful figure of merit as it defines the output gain of the laser beam while taking into account the quality of the focal beam spot in terms of intensity. For the disk amplifier studied, the maximum Strehl ratio efficiency that can be achieved is 7.9. The PSD experimental setup as shown in Fig. 2 can be scaled to a larger array size to solve for higher

order Zernike terms; for our study, we were only interested in the first five Zernike terms; therefore, an array size of 2 × 2 was sufficient.

ACKNOWLEDGMENTS

This work was funded by the EPSRC Centre for Doctoral Training in Applied Photonics (Ref No. 1630477) and also supported in part by the EC through Laserlab-Europe, No. H2020 EC-GA 654148.

APPENDIX: RE-CONSTRUCTION THE WAVE-FRONT PROFILE

The wave-front error can be reconstructed by relating the change in the focal spot position measured using the PSD array and the gradient of the wave-front profile using Eq. (7). The gradient of the wave-front profile in the x and y planes at the central position of the four lenses ($x_{0,n}$, $y_{0,n}$, where **n** is the PSD number) is as follows:

$$\frac{dW(x,y)}{dx}\Big|_{x=x_{0,n},y=y_{0,n}} = 2Z_a + 2\sqrt{6}Z_c y_{0,n} + 4\sqrt{3}Z_d x_{0,n} + 2\sqrt{6}Z_e x_{0,n},$$

$$\frac{dW(x,y)}{dy}\Big|_{x=x_{0,n},y=y_{0,n}} = 2Z_b + 2\sqrt{6}Z_c x_{0,n} + 4\sqrt{3}Z_d y_{0,n} + 2\sqrt{6}Z_e y_{0,n}.$$

A total number of eight equations (four PDSs in x and y) needs to be solved for each step. The eight equations for all four PSDs can be expressed in the matrix form,

$$\begin{bmatrix} 2 & 0 & 2\sqrt{6}y_{0,1} & 4\sqrt{3}x_{0,1} & 2\sqrt{6}x_{0,1} \\ 0 & 2 & 2\sqrt{6}x_{0,1} & 4\sqrt{3}y_{0,1} & 2\sqrt{6}y_{0,1} \\ 2 & 0 & 2\sqrt{6}y_{0,2} & 4\sqrt{3}x_{0,2} & 2\sqrt{6}x_{0,2} \\ 0 & 2 & 2\sqrt{6}x_{0,2} & 4\sqrt{3}y_{0,2} & 2\sqrt{6}y_{0,2} \\ 2 & 0 & 2\sqrt{6}y_{0,3} & 4\sqrt{3}x_{0,3} & 2\sqrt{6}x_{0,3} \\ 0 & 2 & 2\sqrt{6}x_{0,3} & 4\sqrt{3}y_{0,3} & 2\sqrt{6}y_{0,3} \\ 2 & 0 & 2\sqrt{6}y_{0,4} & 4\sqrt{3}x_{0,4} & 2\sqrt{6}x_{0,4} \\ 0 & 2 & 2\sqrt{6}x_{0,4} & 4\sqrt{3}y_{0,4} & 2\sqrt{6}y_{0,4} \end{bmatrix} \begin{bmatrix} Z_a \\ Z_b \\ Z_c \\ Z_d \\ Z_e \end{bmatrix} = \begin{bmatrix} \frac{x'_1 - x_{R,1}}{2f} \\ \frac{y'_1 - y_{R,1}}{2f} \\ \frac{x'_2 - x_{R,2}}{2f} \\ \frac{y'_2 - y_{R,2}}{2f} \\ \frac{x'_3 - x_{R,3}}{2f} \\ \frac{y'_3 - y_{R,3}}{2f} \\ \frac{x'_4 - x_{R,4}}{2f} \\ \frac{y'_4 - y_{R,4}}{2f} \end{bmatrix},$$

where $x_{R,n}$ and $y_{R,n}$ are the initial reference position in the (x, y) -axis. An exact solution that satisfies all eight equations is not possible. Therefore, the least squares fit method was used to fit for the Zernike coefficients Z_a, Z_b, Z_c, Z_d, and Z_e for each time step. To ensure the validity of the fit, a residual error measurement is conducted by inputting the calculated values for Z_a, Z_b, Z_c, Z_d, and Z_e into the matrix and calculating the output $E_{(n,x)}$ and $E_{(n,y)}$,

$$\begin{bmatrix} 2 & 0 & 2\sqrt{6}y_{0,1} & 4\sqrt{3}x_{0,1} & 2\sqrt{6}x_{0,1} \\ 0 & 2 & 2\sqrt{6}x_{0,1} & 4\sqrt{3}y_{0,1} & 2\sqrt{6}y_{0,1} \\ 2 & 0 & 2\sqrt{6}y_{0,2} & 4\sqrt{3}x_{0,2} & 2\sqrt{6}x_{0,2} \\ 0 & 2 & 2\sqrt{6}x_{0,2} & 4\sqrt{3}y_{0,2} & 2\sqrt{6}y_{0,2} \\ 2 & 0 & 2\sqrt{6}y_{0,3} & 4\sqrt{3}x_{0,3} & 2\sqrt{6}x_{0,3} \\ 0 & 2 & 2\sqrt{6}x_{0,3} & 4\sqrt{3}y_{0,3} & 2\sqrt{6}y_{0,3} \\ 2 & 0 & 2\sqrt{6}y_{0,4} & 4\sqrt{3}x_{0,4} & 2\sqrt{6}x_{0,4} \\ 0 & 2 & 2\sqrt{6}x_{0,4} & 4\sqrt{3}y_{0,4} & 2\sqrt{6}y_{0,4} \end{bmatrix} \begin{bmatrix} Z_{a,C} \\ Z_{b,C} \\ Z_{c,C} \\ Z_{d,C} \\ Z_{e,C} \end{bmatrix} = \begin{bmatrix} E_{(1,x)} \\ E_{(1,y)} \\ E_{(2,x)} \\ E_{(2,y)} \\ E_{(3,x)} \\ E_{(3,y)} \\ E_{(4,x)} \\ E_{(4,y)} \end{bmatrix}.$$

To calculate the residual error in the least squares fit method, the change in the focal spot position measured is subtracted from $E_{(n,x)}$ and $E_{(n,y)}$. The residual error between the measured values and the least squares fit method returns a 1 × 8 matrix; therefore, the mean value across all the elements in the ERR matrix gives the total residual error for each time step,

$$E_{(n,j)} - \frac{j_i - j_{R,i}}{2f} = ERR$$

$$ResidualError = \overline{ERR},$$

where $n = 1, \ldots, 4$ and $j = x, y$.

The residual error for the least squares fit method for each time step was taken as the mean value of all the elements in the matrix *ERR*, and it was calculated to be in the region of $\pm 3 \times 10^{-15}$.

REFERENCES

[1] D. Brown, *High-Peak-Power Nd: Glass Laser Systems*, Springer Series in Optical Sciences (Springer Berlin Heidelberg, 2013).
[2] M. Mangir and D. Rockwell, IEEE J. Quantum Electron. **22**, 574 (1986).
[3] M. Weber, *CRC Handbook of Laser Sscience and Ttechnology* (CRC Press, 1987).
[4] W. Koechner, *Solid-State Laser Engineering*, Springer Series in Optical Sciences (Springer Science & Business Media, 2006).
[5] C. Hernandez-Gomez, J. L. Collier, S. J. Hawkes, C. N. Danson, C. B. Edwards, D. A. Pepler, I. N. Ross, and T. B. Winstone, Appl. Opt. **39**, 1954 (2000).
[6] V. Ramanathan, J. Lee, S. Xu, X. Wang, L. Williams, W. Malphurs, and D. H. Reitze, Rev. Sci. Instrum. **77**, 103103 (2006).
[7] B. M. Van Wonterghem, J. R. Murray, J. H. Campbell, R. D. Speck, C. E. Barker, I. C. Smith, D. F. Browning, and W. C. Behrendt, Appl. Opt. **36**, 4932 (1997).
[8] S. B. Sutton, A. Erlandson, R. A. London, K. R. Manes, and C. D. Marshall, Proc. SPIE **3492**, 665–675 (1999).
[9] K. C. Widen and R. J. Tansey, Proc. SPIE **1868**, 413–418 (1993).
[10] V. N. Mahajan, J. Opt. Soc. Am. **73**, 860 (1983).
[11] H. Zhu, Q. Lou, and S. He, Opt. Eng. **44**, 094205 (2005).
[12] M. Kumar, C. Narayanamurthy, and A. Kumar, Opt. Eng. **53**, 064102 (2014).
[13] I. Weingaertner and M. Schulz, Proc. SPIE **1781**, 266–279 (1993).
[14] P. Sikocinski, O. Novak, M. Smrz, J. Pilar, V. Jambunathan, H. Jelínková, A. Endo, A. Lucianetti, and T. Mocek, Appl. Phys. B **122**, 73 (2016).
[15] R. Ragazzoni, J. Mod. Opt. **43**, 289 (1996).
[16] V. Akondi, S. Castillo, and B. Vohnsen, Opt. Express **21**, 18261 (2013).
[17] H. Wang, C. Liu, X. He, X. Pan, S. Zhou, R. Wu, and J. Zhu, High Power Laser Sci. Eng. **2**, e25 (2014).
[18] V. Lakshminarayanan and A. Fleck, J. Mod. Opt. **58**, 545 (2011).